5.5 Materials Science

In the field of the materials science, some kinds of x-ray diffraction/scattering methods are utilized.

One of the most famous methods is "Resonant X-ray Scattering" as follows:

Anisotropic Resonant X-Ray Scattering from Anti-ferromag net Hematite, Fe_2O_3

Anisotropic resonant X-ray scattering is a useful method for studying local electronic states in a crystal. Up until now, however, very little experimental work on this scattering has been reported. The present work is a basic study of resonant X-ray scattering in a magnetic material.

Anisotropic resonant scattering is described by the anisotropic tensor of susceptibility (ATS). In general ATS scattering is very small compared with charge scattering, but it can be measured using a forbidden refl ection, since the anisotropic tensors violate the conventional extinction rule for Bragg reflection. Resonant diffraction is sensitive to the X-ray energy and allows us to investigate a specific atom in a crystal. ATS scattering is furthermore dependent on the X-ray polarization and is sensitive to the atomic direction, i.e. the electronic orbital. Using this scattering we can obtain information about the local anisotropy of the unoccupied electronic states.

The electric dipole approximation is usually applied to the resonant (or anomalous) scattering factor. In some samples (Fe_2O_3, FeS_2 etc.), however, the quadrupole transition effect has been observed in ATS scattering [1,2]. It is important whether the quadrupole effect is observed or not in resonant X-ray phenomena. We can obtain more detailed information on the electronic states

from the observation of the higher order effect. On the other hand, magnetic X-ray scattering also shows anisotropic properties. Therefore magnetic scattering should be taken into account in the scattering from magnetic materials. In principle we can obtain the spin and orbit magnetization densities from non-resonant magnetic scattering, while resonant magnetic scattering gives us information on the magnetically ordered electronic tates.

We have selected as a sample, the antiferromagnet hematite, Fe_2O_3, which has a corundum structure and a magnetic moment almost perpendicular to the three-fold rotation axis (the hexagonal [001] direction) at room temperature. In order to clarify the resonant scattering process in hematite, we have investigated the forbidden reflections near the Fe K-absorption edge. The experiment was carried out with four-circle diffractometers at BL-3A and 4C, where the incident beam was polarized horizontally and the scattering plane was perpendicular to it, i.e. σ-polarized. The integrated intensity was measured for the hexagonal 003 and 009 forbidden reflections at different X-ray energies or azimuthal angles.

We first measured the energy spectra of the 003 and 009 forbidden reflections intensities. These spectra have only one peak (7.105 keV) at the same energy in the pre-edge region and there is a small non-resonant intensity below the edge. Above the edge, however, manifest nonresonant intensity was not observed because of large absorption.

The azimuthal angle dependence of the forbidden reflections measured at the non-resonant energy, 7.085 keV, shows a twofold pattern (Fig. 1) in spite of the three-fold rotation axes at the iron sites. This property can be explained by non-resonant magnetic scattering due to the antiferromagnetic moment in the (00*l*) plane. At the
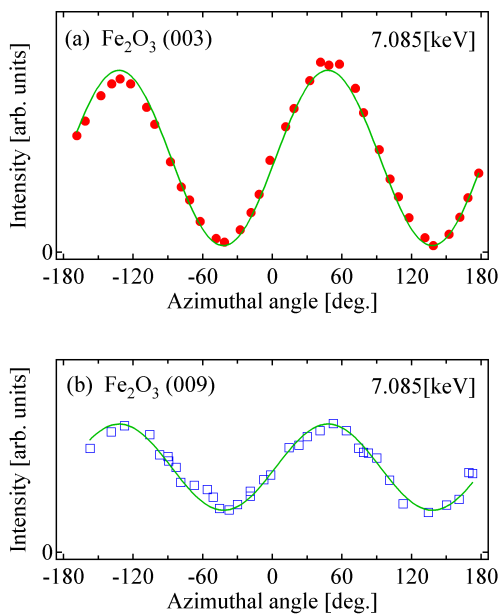

Figure 1
Azimuthal angle dependence of the 003 and 009 reflections in hematite at a non-resonant energy. The solid lines are calculated based on non-resonant magnetic scattering.
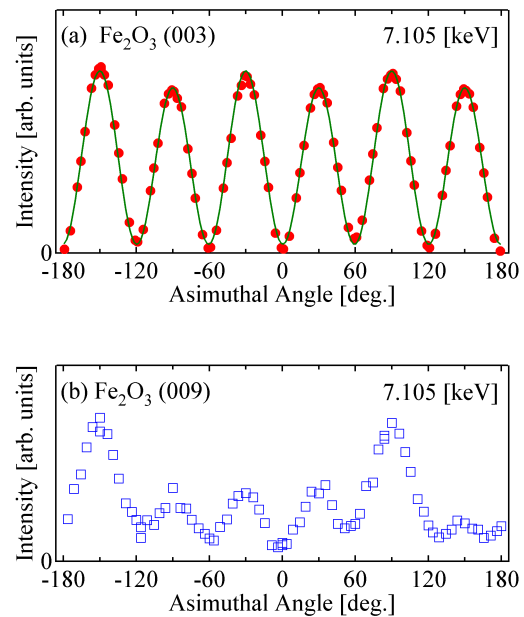

Figure 2
Azimuthal angle dependence of the 003 and 009 reflections in hematite at the resonant peak energy. The solid line is calculated from electric dipole-quadrupole and quadrupole-quadrupole transition

resonant peak energy, on the other hand, the threefold pattern is observed in the 003 reflection, where a local maximum is a little different from the neighboring one as shown in Fig. 2(a). This character is explained by the electric dipole-quadrupole and quadrupole-quadrupole transition as shown in Fig. 2(a). Finally the azimuthal dependence of the 009 reflection at the resonant energy scarcely shows threefold symmetry as shown in Fig. 2(b). This phenomenon cannot be explained by only the electric multipole transition process, which should satisfy the usual point symmetry. The non-resonant magnetic scattering contribution also cannot account for this property because its intensity is smaller than that of the resonant one by about ten times. Therefore we conclude that the resonant 009 reflection may be affected by the resonant magnetic scattering with different scattering process.

References

[1] K.D. Finkelstein *et al.*, *Phys. Rev. Lett.* **69** (1992) 1612.
[2] J. Kokubun *et al.*, *J. Phys. Soc. Jpn.* **67** (1998) 3114.

This technique is utilized for Mn oxide thin film. These experimental technique take a new turn for material science as follows;

A New Experimental Technique Using Resonant X-Ray Scattering; Observation of Ferro-Type Orbital Ordering and Elucidation of its Scattering Mechanism

Manganese 3d orbital states in thin films and superlattices have been investigated by a newly developed technique [3, 4]. Here "orbital state" means the orbital occupancy of 3d electrons and their spatial arrangements. These artifi cial materials are expected to demonstrate "orbital-state-mediated phase-control". For the characterization of these materials, accurate examinations of the orbital states are indispensable. The resonant X-ray scattering (RXS) technique has been proved to be a very powerful probe of the orbital states, and now is being applied to a wide range of systems with improved accuracy. The newly developed interference technique has enabled the observation of ferro-type orbital ordering whose signal coincides with fundamental Bragg reflections at Γ points. This method utilizes the interference term between X-rays scattered with RXS and those from Thomson scattering. This term can be extracted from rotation of the polarization. Using the interference technique, we have succeeded in inspecting the orbital states of thin films. Furthermore, we have successfully observed an "orbital superlattice", in which manganese 3d orbital states are periodically modulated on an atomic scale.

Perovskite manganite $La_{0.5}Sr_{0.5}MnO_3$ (LSMO) thin films epitaxially grown on three kinds of single crystalline perovskite substrates were investigated. The hetero junction between the film and the substrate induces a coherent epitaxial strain in the film whose in-plane
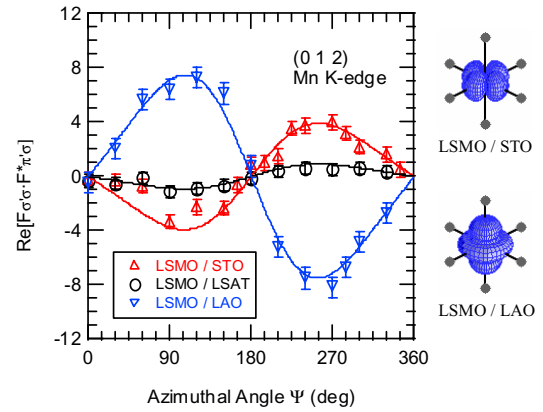

Figure 3
The azimuthal angle dependence of the interference term intensity. Data for the fi lms on STO, LSAT, and LAO are presented as a function of the azimuthal angle Ψ (left). e_g orbitals of LSMO/STO and LSMO/LAO samples are shown (right).

lattice parameter is forced to match to that of the substrate. Macroscopic properties such as conductivity and/or magnetization suggest that the orbital states of LSMO films vary with substrate according to the coherent strains present, that is, those on $SrTiO_3$ (STO), $(LaAlO_3)_{0.3}(SrAl_{0.5}Ta_{0.5}O_3)_{0.7}$ (LSAT) and $LaAlO_3$ (LAO) take $d_{x^2-y^2}$, unpolarized and $d_{3z^2-r^2}$ types of e_g orbitals, respectively [5]. Fig.3 shows the azimuthal angle dependence of the interference term intensity of the (0 1 2) fundamental reflections. The variance among the three films is clearly seen, and the polarization of the e_g orbitals can be experimentally distinguished by the sign of the interference term. This technique was also applied to the investigation of orbital states in the $La_{0.45}Sr_{0.55}MnO_3/La_{0.6}Sr_{0.4}MnO_3$ multilayers [6]. Orbital modulation at the interface of superlattice structure is a completely unexplored subject, and the heterojunction of different orbital states may lead to new physical phenomena. We have successfully observed RXS reflections from the present manganite superlattice by using the interference technique. By analyzing the intensity of the interference term at each reflection, it is clearly demonstrated that the polarization of the e_g orbitals differs in each layer, presenting an "orbital superlattice". Figure 4 shows the expected e_g orbital state in this manganite superlattice.

The interference technique also brought about important information on the mechanism of RXS. RXS probes the 4p electronic states of Mn atoms by using X-rays tuned to the manganese K-absorption edge. As for the origin of the 4p level splitting, two explanations are possible: one ascribes it to the Coulomb interaction between Mn 3d and 4p states, the other to the hybridization between Mn 4p and O 2p orbitals. These two mechanisms give an opposite sign to the interference term, and the origin of the 4p level splitting is determined by the interference technique. Our results confirm that the origin of the RXS in manganites is mainly attributable to the hybridization between Mn 4p and O 2p orbitals, and not to the Coulomb interaction between the 3d and 4p electronic states.

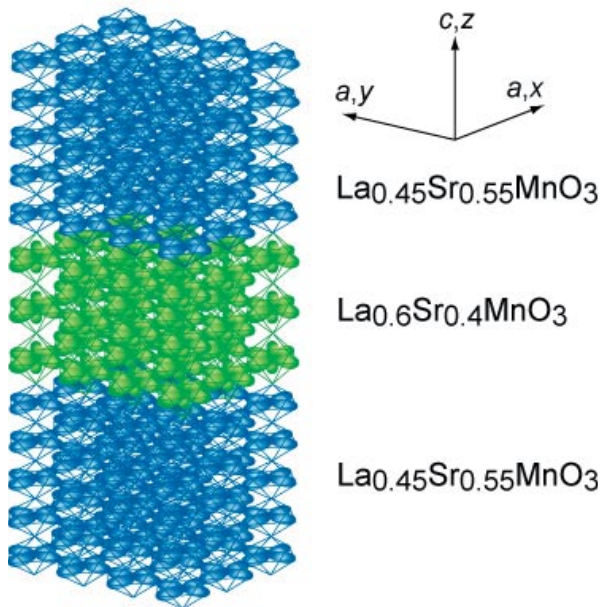Thus, the newly developed RXS technique has en-

Figure 4
Schematic of e_g orbital states in the [La$_{0.45}$Sr$_{0.55}$MnO$_3$ 10u.c./ La$_{0.6}$Sr$_{0.4}$MnO$_3$ 3u.c.]$_{20}$ "orbital superlattice". (x^2–y^2)-type orbitals in the La$_{0.45}$Sr$_{0.55}$MnO$_3$ layers and (x^2–y^2)/($3z^2$–r^2) disordered orbitals in the La$_{0.6}$Sr$_{0.4}$MnO$_3$ layers are presented.

abled not only the observation of ferro-type orbital ordering, but also the clarification of the mechanism of RXS.

References

[3] T. Kiyama, Y. Wakabayashi, H. Nakao, H. Ohsumi, Y. Murakami, M. Izumi, M. Kawasaki and Y. Tokura, *J. Phys. Soc. Jpn.*, **72** (2003) 785.

[4] H. Ohsumi, Y. Murakami, T. Kiyama, H. Nakao, M. Kubota, Y. Wakabayashi, Y. Konishi, M. Izumi, M. Kawasaki and Y. Tokura, *J. Phys. Soc. Jpn.*, **72** (2003) 1006.

[5] Y. Konishi, Z. Fang, M. Izumi, T. Manako, M. Kasai, H. Kuwahara, M. Kawasaki, K. Terakura and Y. Tokura, *J. Phys. Soc. Jpn.*, **68** (1999) 3790.

[6] M. Izumi, T. Manako, Y. Konishi, M. Kawasaki and Y. Tokura, *Phys. Rev. B,* **61** (2000) 12187.

"Devil's Flower" Blooming in NaV$_2$O$_5$

The most exciting phase diagram in statistical physics -*Devil's Flower* [7] - has been reproduce dexperimentally in the Temperature-Pressure (*T-P*) phase diagram of NaV$_2$O$_5$ [8].

In 1985, Bak *et al.* proposed a simple model, which is well known as the ANNNI (Axial Next Nearest Neighbor Ising) model at present. On the basis of such a model, they carried out theoretical calculations considering two competitive inter-layer interactions between Ising spins (see Fig. 5 inset), i.e., the nearest neighbor interaction $J_1>0$ (ferro) and the next nearest neighbor interaction $J_2<0$ (antiferro) and obtained an interesting κ-T ($\kappa = -J_2/J_1$) phase diagram (see Fig. 5) in which an infinite number of commensurate phase appears as a function of κ and T. Such a phase diagram is named *"Devil's Flower"*, because it seems as if an infinite number of petals bloom from the $\kappa = 0.5$ position.

A quarter-filled spin-ladder system NaV$_2$O$_5$ undergoes a novel cooperative phase transition associated at Tc = 34 K with its charge ordering, lattice dimerization

(2a×2b×4c superstructure) and spin-gap formation. By the complementary use of synchrotron X-ray structural analysis and resonant X-ray scattering (RXS) techniques at the Photon Factory, the 2a×2b×4c superstructure below Tc was solved unambiguously [9,10]. An oblique charge stripe pattern formed in each V$_2$O$_5$- layer (*ab*-plane) is shown in Fig. 6 as A and A'. Atomic shifts coupled with such a charge ordering are not shown in this figure. The charge ordering patterns called A and A' are related by a phase shift π along the b-axis, where a dark blue colored pyramid represents V^{4+}O$_5$ and a light blue V^{5+}O$_5$. The stacking sequence of the patterns A and A' along the c-axis was unambiguously determined by the RXS as AAA'A' [10].

By application of high pressure, the stacking sequence along the c-axis drastically changes. For an overall study, we applied an oscillation photographic method (BL-1B), and for a detailed study, we used a
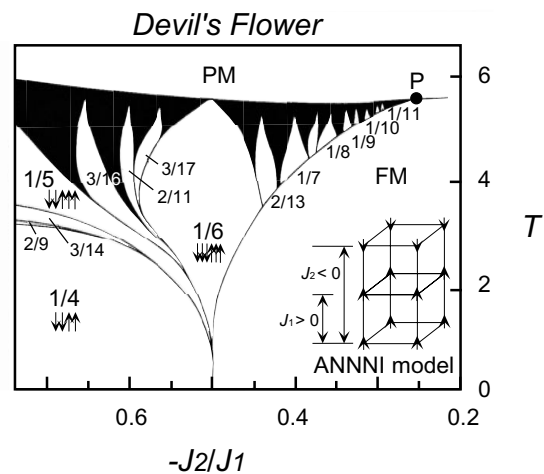

Figure 5
"Devil's Flower" (κ-T phase diagram) obtained from ANNNI model. Fractions seen in the phase diagram show the modulation wave numbers. Black regions are composed of more complicated commensurate and incommensurate phases.
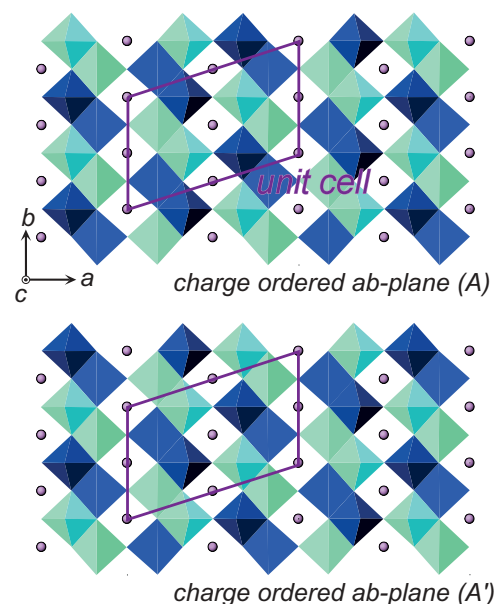

Figure 6
Schematic charge order patterns determined in *ab*-plane, consisting of two kinds of patterns A and A'.

counter method (BL-4C). Figure 7(a) presents the temperature dependence of the [15/2, 1/2, q_c] superlattice Bragg position at 0.88 GPa taken at BL-1B. One can clearly see that the modulation wave number q_c changes as a function of temperature. Figure 7(b) displays the temperature dependence of *high-resolution* diffraction profiles observed along the [13/2, 3/2, q_c] direction at 0.92 GPa taken at BL-4C. In this figure, a few more reflections are newly observed. It is also shown that a series of superlattice reflections with q_c = 1/4, 1/5, 1/6 and 3/17 systematically appear and disappear as a function of temperature. What we observe is peak intensities coming from the atomic shifts coupled with the charge modulations [11]. This qc sequence means that the stacking sequence along the c-axis drastically changes as AAA'A'A' for 1/5, AAAAA'A'A' for 1/6, AAA'A'A'AAAA'A' A'AAAA'A'A' for 3/17 and so on. We also could observe the other types of qc sequences in a wide temperature and pressure range and fi nally confi rmed that the "*Devil's Flower*" is perfectly reproduced in NaV_2O_5 [8] under high pressure and low temperature (Fig. 8). A microscopic mechanism of the competitive inter-layer interaction resulting in such a phase diagram is a keen subject of further study.

References

[7] P. Bak and J. von Boehm, *Phys. Rev.,* **B 21** (1980) 5297.

[8] K. Ohwada, Y. Fujii, N. Takesue, M. Isobe, Y. Ueda, H. Nakao, Y. Wakabayashi, Y. Murakami, K. Ito, Y. Amemiya, H. Fujihisa, K. Aoki, T. Shobu, Y. Noda and N. Ikeda, *Phys. Rev. Lett.,* **87** (2001) 086402.

[9] H. Sawa, E. Ninomiya, T. Ohama, H. Nakao, K. Ohwada, Y. Murakami, Y. Fujii, Y. Noda, M. Isobe and Y. Ueda, *J. Phys. Soc. Jpn.* **71** (2001) 385; H. Sawa, *Photon Factory Activity Report* **2000 #18** (2001) A 25.

[10] Y. Katsuki, *Master Thesis (Graduate School of Science, The University of Tokyo, Mar. 2002)*; Y. Fujii *et al. in preparation.*

Figure 8
Experimentally obtained T-P phase diagram *"Devil's Flower"* of NaV_2O_5. The hutched area shows commensurate phases unambiguously identified while the shaded area indicates more complicated higher-order commensurate or incommensurate phases.

[11] K. Ohwada *et al. private communication.*

Magnetic Control of Ferroelectric Polarization

Materials showing both magnetic and ferroelectric orders are called "magnetic ferroelectrics" (recently referred to as *magnetoelectric multiferroics)*, in which the coupling between the electric and magnetic polarization is anticipated to give an additional degree of freedom in magnetoelectric and magnetooptical device design. However, there have been few exploratory studies, due to the limited availability of materials and the small magnitude of the effect.
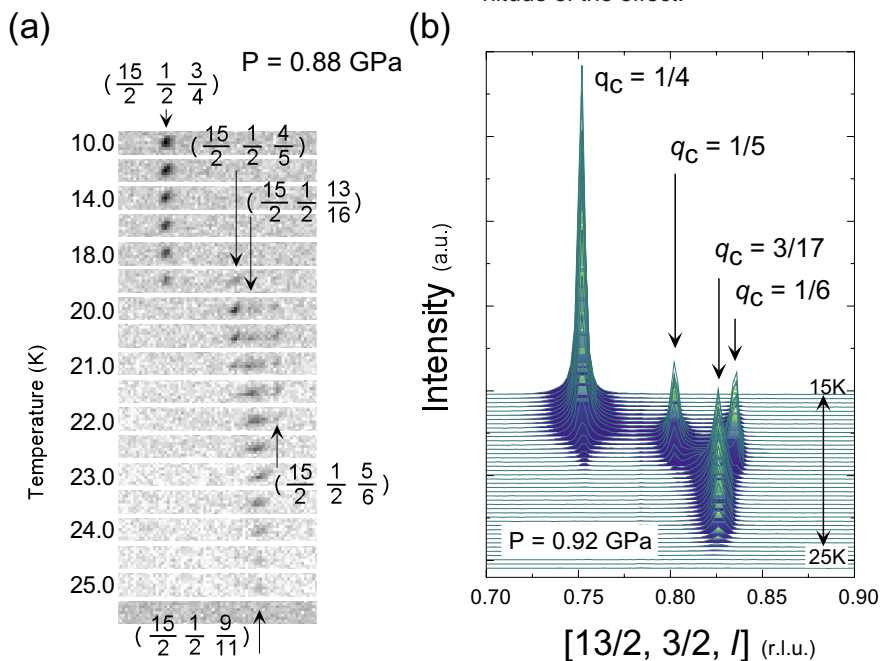

Figure 7
(a) Temperature dependence of a position of superlattice reflections *(15/2, 1/2 l)* recorded on IP oscillation photographs at 0.88 GPa. (b) Temperature dependence of high-resolution X-ray diffraction profiles observed along the [13/2, 3/2, q_c] direction at 0.92 GPa.
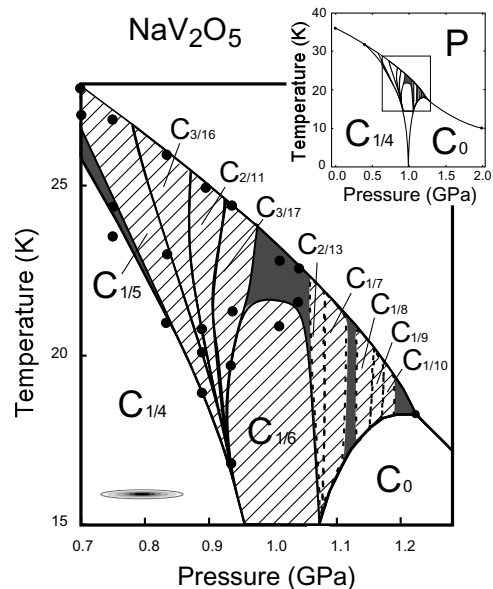
We have discovered gigantic magnetoelectric and magnetocapacitive effects as well as ferroelectricity in some rare-earth manganites [12,13], providing a novel approach to attaining mutual control between magnetism and ferroelectricity. The rare-earth manganites we investigated ($TbMnO_3$ and $DyMnO_3$) have an orthorhombically distorted perovskite structure (with space group *Pbnm*) at room temperature, and show a sinusoidal antiferromagnetic ordering of the Mn^{3+} moments below $T_N \sim 40$ K with a wave vector q = $(0,k_s,1)$. Crystallographic and magnetic structures for $TbMnO_3$ are illustrated in Fig. 9(a). At lower temperatures (TC), ferroelectric order with spontaneous polarization along the c axis appears, as shown in Fig. 10(d).

X-ray diffraction measurements at BL-4C have revealed the lattice distortion producing the polar structures and the relationship between magnetism and ferroelecricity in the rare-earth perovskite manganites [12,14]. Figure 10(a) and (b) show X-ray diffraction scans along $(0,k,3)$ at various temperature for $TbMnO_3$ and $DyMnO_3$ crystals. For both crystals, additional superlattice peaks appear at the wave vector $(0,k_l,l)$ for integer l at temperature below T_N. Figure 10(c) shows the temperature dependence of wave number kl and normalized intensity of superlattice refl ection at $(0,k_l,3)$ attributed to the lattice modulation. For both $TbMnO_3$ and $DyMnO_3$, k_l is temperature-dependent just below T_N, but is locked-in below T_c [Fig. 10(c)]. The value of k_l is almost twice as large as that of k_s, as illustrated in Fig. 9(b). It is well-known that crystallographic deformations at magnetic ordering are due to the exchange striction. The observed superlattice refl ections due to the atomic displacement can be regarded as the second harmonic peaks magnetoelastically induced by sinusoidal antiferromagnetic order.

The close relationship between lattice modulation and ferroelectricity is common to the so-called improper ferroelectrics (e.g. K_2SeO_4, Rb_2ZnCl_4), where the primary order parameter represents the lattice distortion mode having nonzero wave vector (that is $k_l = 0$), and the spontaneous polarization appears as a secondary order parameter induced by the lattice distortion. This may also be the case for the perovskite rare-earth manganites. These observations show that the ferroelectricity in these manganites ordinates in magnetic interactions, through magnetoelastically-induced lattice modulations. Supporting this view, we observed a fas-

(a)

a → *b*

c → *b*

(b) Magnetic and lattice modulations at $T < T_N$
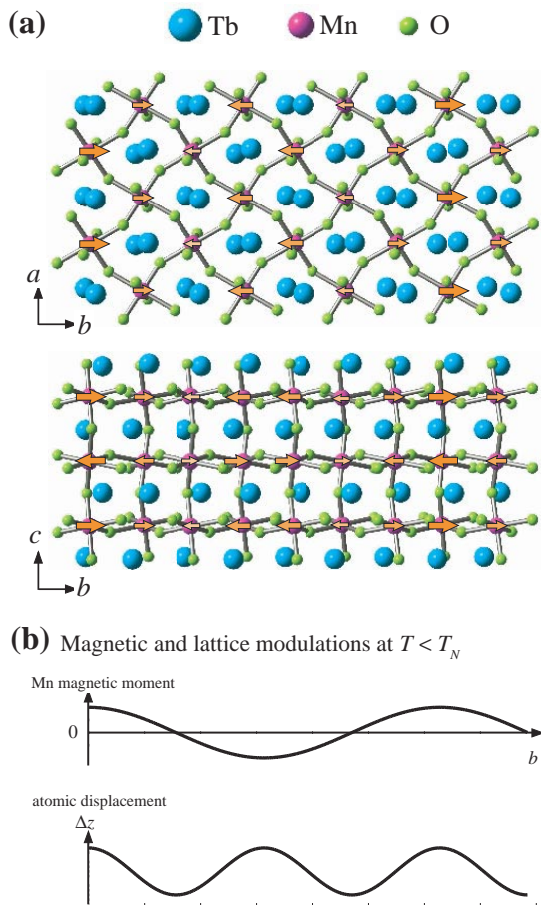
Mn magnetic moment

atomic displacement
Δz

Figure 9
(a) Sketches of crystal structure at room temperature and (b) spatial variation along the b-axis of Mn magnetic moment and atomic displacement (Δz//c) below T_N in $TbMnO_3$. Orange arrows denote Mn magnetic moments below T_N .
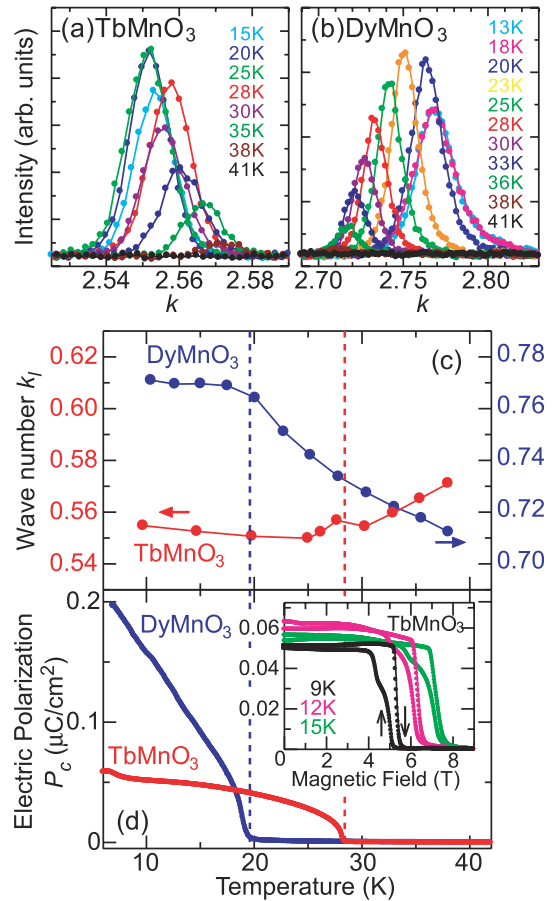

Figure 10
X-ray diffraction *k*-scans along $(0,k,3)$ at various temperatures for single crystals of (a) $TbMnO_3$ and (b) $DyMnO_3$. Temperature profi les of (c) wave vector of lattice modulation k_l and (d) electric polarization along the *c* axis in single crystals of $TbMnO_3$ and $DyMnO_3$. The dashed lines denote the lock-in (ferroelectric) transition temperature. Inset: Electric polarization along the *c* axis as a function of magnetic field at selected temperatures for $TbMnO_3$.

cinating magnetoelectric coupled phenomenon, which we call "magneticfield induced electric polarization flop" [12,13], where the direction of the ferroelectric polarization can be switched from the *c* to the *a* axis by the application of a magnetic fi eld [inset of Fig. 10(d)]. These results provide a path to new magneto-electric applications.

References

[12] T. Kimura, T. Goto, H. Shintani, K. Ishizaka, T. Arima and Y. Tokura, *Nature* (London), **426** (2003) 55.

[13] T. Kimura, S. Ishihara, H. Shintani, T. Arima, K. T. Takahashi, K. Ishizaka and Y. Tokura, *Phys. Rev. B,* **68** (2003) 060403(R).

[14] T. Goto, T. Kimura, G. Lawes, A. P. Ramirez and Y. Tokura, *Phys. Rev. Lett.*, **92** (2004) 257201.

An X-ray Micro Diffraction Analysis of the Dynamic Local Layer Response to an Electric Field in Ferroelectric Liquid Crystals

Liquid crystal research has become an interdisciplinary field having practical applications. Among the various phases of liquid crystals, the smectic C (SmC) phase is characterized by a one-dimensional order and that a rodlike molecule tilts with respect to the layer normal. Ferroelectricity in liquid crystals was fi rst observed in the chiral SmC* phase followed by the discovery of its fast electrooptic switching. In the last ten years, antiferroelectricity and intermediate ferrielectric phases have been found and systematic research into the chiral smectic phase of (anti-)ferroelectric liquid crystals [(A)FLCs] has been intensively performed, though the origin of these phases is still unclear. In order to understand the electro-optical response of the (A)FLC, analysis of the static and dynamic layer structure in an electric fi eld is crucial. Since the SmC* phase in an electric fi eld shows a characteristic texture observable by an optical microscope, X-ray icrobeams are indispensable for its study. Recently, timeresolved synchrotron X-ray micro-diffraction has been applied to the characterization of the local layer structure of the SmC* phase, revealing the dynamic as well as the static layer structure [15].

BL-4A was used for the micro-diffraction experiment (3 × 4 μm^2 focus size). The diffracted intensities were measured as a function of angles ω and χ, which correspond to the layer orientation with respect to the rubbing direction normal and the surface normal, respectively. Time resolved measurements were performed with a time resolution of a few μs. The samples were homogeneously aligned TK-C101 (FLC, Chisso) sandwiched between Indium Tin Oxide (ITO)-coated glass plates, and the cell gap was 7.5 μm.

The irreversible layer transformation under increasing electric fi eld consisted of two stages. With an applied field of AC the initial vertical-chevron (v-chevron) structure transformed to an alternating vertical and horizontal chevron structure [Fig. 11(a)]. Further increasing the fi eld, the chevron angle decreased and a horizontal

chevron (h-chevron) structure developed [Fig. 11(b) and (c)]. Corresponding optical micrographs show the generation [Fig. 11(d)], development [Fig. 11(e)] and the modifi cation [Fig. 11(f)] of the stripe texture. The time-resolved microdiffraction measurement has clarifi ed the detailed reversible layer transformation. Figures 12(a) and (b) show the time resolved ω- and χ-profiles for the triangular wave form applied field. At low voltage, the ω - and χ-profile shows a double peak. At high voltage, a single peak appears in the ω-profile while a double peak with a relatively large angular separation is seen in the χ-profile. Since the profi le changes periodically from position to position, it is concluded that the local layer transforms between a mostly h-chevron with a small portion of the v-chevron structure at high fi eld [Fig. 12(c)] and the so-called quasibookshelf structure at the low field. This layer transformation can be explained in terms of the electric torque and surface anchoring. At high fi eld, the electric torque due to the interaction between the electric field and the spontaneous polarization makes the layer upright, while surface anchoring due to the rubbed alignment fi lm tends to form the v-chevron structure. The local layer structure at high fi eld is due to the competition between these two forces. The transient response time of the local layer for the square wave form was measured for the first time. The layer responds to the external field quickly within 0.1~0.4 ms; this was found to be slightly longer than the optical response time.

Reference

[15] Y. Takahashi, A. Iida, Y. Takanishi, T. Ogasawara, M. Nakata, K. Ishikawa and H. Takezoe, *Phys. Rev. E,* **67** (2003) 051706.
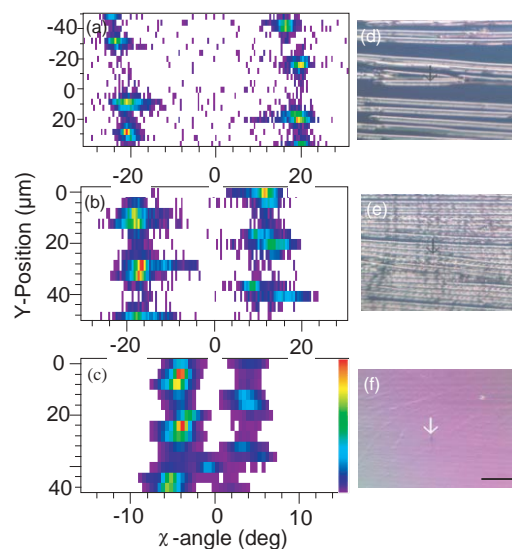
Figure 11
Series of χ-profiles (a)~(c) and corresponding polarized optical micrographs of FLC texture (d)~(f) under an AC electric field. Applied voltages are ±18 V (a) and (d), ±30 V (b) and (e), and ±60 V (c) and (f). A scale mark in (f) represents 100 μm

Figure 12

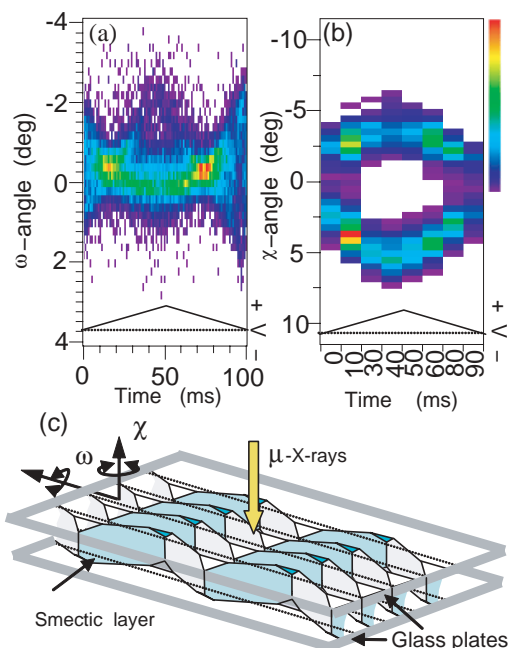Time resolved ω-profiles (a) and χ-profiles (at ω ~ 0°) (b) for a half cycle of the applied triangular wave form electric field (5 Hz, ±60V). The lower insets show the applied wave form. (c) A schematic representation of the possible local layer structure at high electric field.

Formation of Ice Nanotubes inside Carbon Nanotubes

It is well known that the physical properties of water are almost independent of volume, changing only gradually in the bulk scale region. When the volume decreases below the few-molecule size, however, water exhibits quite different properties compared to the bulk scale. Such waters exist everywhere on earth and play important roles in the occurrence of various phenomena. Recently, we have found that water confined inside single-walled carbon nanotubes (SWCNTs) with onedimensional hollow cavities of diameters of 8 to 12 Å display interesting structural properties [16,17] which cannot be extrapolated from the macroscopic scale.

Diameter-controlled SWCNT samples were examined by means of detailed X-ray diffraction (XRD) structural analysis conducted at BL-1B. Fig. 13 shows the typical temperature dependence of the XRD patterns from an SWCNT sample. It was found that water was easily adsorbed inside the SWCNTs at room temperature, and a new form of ice, "ice nanotubes" (ice-NT) was formed at lower temperatures. Figure 14 illustrates one example of the observed ice-NT structures, pentagonal ice-NT, where the water molecules form *n*-membered rings, through hydrogen bonds. (Here *n* represents an integer.) These rings stack one-dimensionally to form *n*-membered ice-NTs inside the SWCNT. While the possibilty of ice-NT formation was predicted by Koga *et al.* in 2001 using molecular dynamics calculations for water confined inside SWCNT by axial pressures of 50 to 500 MPa [18], the present experiments show that ice-NTs can be formed without applying high pressures. With increasing SWCNT diameter, ice-NTs with larger
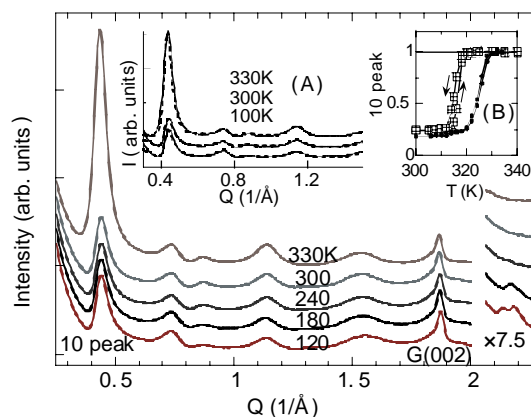

Figure 13

Temperature dependence of the XRD patterns of a SWCNT sample with an average diameter of 13.5 Å. The small peaks at $Q \sim 2.2 \text{Å}^{-1}$ are assigned to the ice-NTs. The peaks denoted with G(002) are due to graphite-like impurities. Inset (A): Comparison of the observed and simulated XRD patterns after background-removal. Inset (B): Temperature dependences of the 10 peak intensity at $Q \sim 0.45 \text{Å}^{-1}$ for two SWCNT samples with different diameters. The larger and smaller squares are for 13.5 and 11.7 Å diameter SWCNT samples, respectively. The steep decreases below around 320 K are evidence for the adsorption of water inside the SWCNTs.
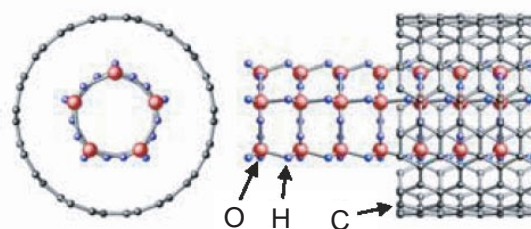

Figure 14

A schematic illustration of pentagonal (5-membered) ice-NT formed inside an SWCNT. The melting point is 300 K.
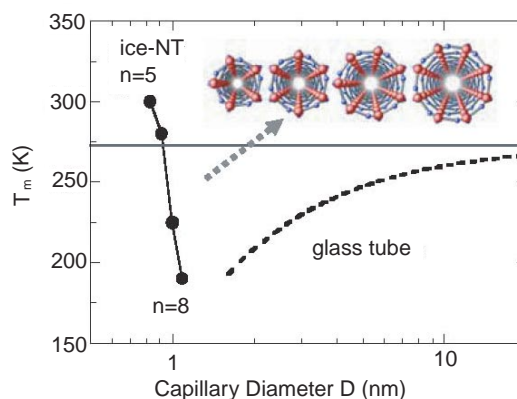

Figure 15

The melting point of ice-NT as a function of the cavity diameter of the SWCNT. The dashed line is the melting point of water confined inside a glass tube extrapolated from the bulk region. The inset shows schematic views of 5 to 8-membered ice-NTs, looking along the tube-axis.

n were more preferentially formed. It was also found that there the melting point of the ice-NTs varies greatly depending on the SWCNT diameter, with smaller diameters leading to higher melting points. This is contrary to existing empirical rules (see Fig. 15). In particular, water in SWCNTs with diameters of 11.7 Å was found to crystallize at 300K or lower. In other words, we have succeeded in forming the fi rst room-temperature ice-NTs at pressures below 0.1 MPa (1 atm). Moreover, we have discovered that the water inside an SWCNT vaporizes at around 320 K and is subsequently ejected, leading to the possibility of a number of applications, including nano-size inkjet printing.

References

[16] Y. Maniwa, H. Kataura, M. Abe, S. Suzuki, Y. Achiba, H. Kira and K. Matsuda, *J. Phys. Soc. Jpn.*, **71** (2002) 2863.

[17] Y. Maniwa, H. Kataura, M. Abe, A. Udaka, S. Suzuki, Y. Achiba, H. Kira, K. Matsuda, H. Kadowaki and Y. Okabe, *Chem. Phys. Lett.*, **401**, (2005) 534.

[18] K. Koga, G. T. Gao, H. Tanaka and X. C. Zeng, *Nature,* **412** (2001) 802.

White X-Ray Magnetic Diffraction of Ferromagnets at BL-3C3

White X-ray magnetic diffraction [19] (WXMD) is a unique method that can measure spin- and/or orbital-magnetic form factors of ferromagnets independently. This method utilizes white X-rays of elliptically polarized synchrotron radiation emitted from a bending magnet out of the electron orbit plane of a storage ring. The accuracy of the measurements is dependent on the emittance and stability of the electron beam in the storage ring. A second-generation low-emittance ring may be suitable for this experiment because of a good balance of adequately low emittance and high stability of the electron beam; one such ring is that of the Photon Factory. The advantage of the white X-ray method over a monochromatic X-ray method is that the magnetic form factors at plural reciprocal-lattice points are measured simultaneously in a measurement. The disadvantage is that the measurements are affected by fluorescent radiation from a specimen and multiple scattering at the specimen.

Beamline BL-3C3 is equipped with a five-circle diffractometer that is optimized to the WXMD experiment and minimizes the above disadvantageous effects. An electromagnet and a refrigerator are installed in the diffractometer. We have some choices of the magnetic-field strength and the temperature of the specimen. Typical cases are: (1) 1.0 tesla and room temperature, (2) 0.4 tesla and temperatures as low as 20 K (using a refrigerator of the He gas circulating type), and (3) 0.3 tesla and temperatures as low as 5 K (using a refrigerator of liquid He flowing type). We have three choices for the magnetic field directions: (a) parallel to the incident beam, (b) parallel to the diffracted beam, and (c) parallel to the scattering vector. Configurations (a), (b) and (c) give us the magnetic form factors of the orbital moment only (that is, the orbital-magnetic form factor), those of the total (spin+orbital) moment (that is, the total magnetic form factor), and those of the spin moment only (that is, the spin-magnetic form factor), respectively, with the 90 degree scattering angle.

In the present study we applied the WXMD method to measure the spin-magnetic form factor of ferromagnetic $YTiO_3$. $YTiO_3$ has a crystal structure of the perovskite type and exhibits orbital ordering of the 3d electrons of Ti atoms [20,21]. This compound is ferromagnetic below 28 K. Polarized neutron diffraction [22] and the resonant X-ray scattering [23] were performed and provided models of the ordered orbitals. The spin- and/or orbital- magnetic form factors measured by the WXMD experiment will give us complementary information about the ordered orbitals.

The specimen crystal was provided by Dr. Y. Taguchi and Prof. Y. Tokura. Preliminary measure ments of the magnetization of the specimen crystal showed that 0.3 tesla is sufficient to saturate the magnetization when the magnetic field is applied along the easy axis of [001]. Because the magnetization was aligned along the [001] axis and the reflection plane was (001) with a scattering angle of 90 degrees (the above (c) configuration), the spin-magnetic form factor was selectively measured. The experimental setup is shown in Fig. 16. We measured the change in the diffraction intensity accompanied by reversing the magnetization direction, so-called the flipping ratio, and obtained the spin-magnetic form factor ($\mu_S(k)$) of the reciprocal lattice points of 006, 008, 0010, and 0012. The results are shown in Fig. 17. The

Figure 16
Experimental setup of the white X-ray magnetic diffraction of $YTiO_3$: a, five-circles diffractometer; b, refrigerator of liquid He-flowing type to keep the temperature of the specimen at 5 K; c, electromagnet producing 0.3 tesla at a gap length of 50 mm; d, slit for receiving diffraction beam and minimizing fluorescent radiation from the specimen; e, pure Ge solid state detector; f, vessel of liquid He; g, transfer tube of liquid He.
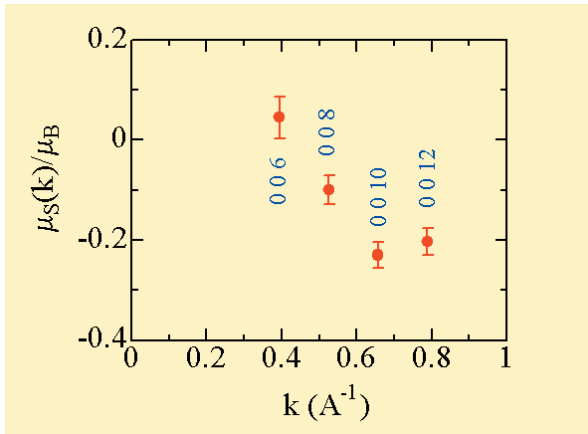
Figure 17
Observed spin-magnetic form factor ($\mu_s(k)$) of $YTiO_3$ at 5 K for reciprocal lattice points of 006, 008, 0010 and 0012. $k=\sin \theta / \lambda$ where θ is the Bragg angle and λ is the X-ray wavelength. μ_B is the Bohr magneton.

observed spin-magnetic form factor shows almost negative values. This result is different from those of other 3d transition metal elements of Fe, Ni and Co which show almost positive values of the magnetic form factors for the magnitude of the scattering vectors in Fig. 17. The obtained spin-magnetic form factor should be related to the ordered orbital of the 3d electrons of Ti atoms. Further analyses and experiments are needed to elucidate the ordered orbital through the observed spin-magnetic form factors. The present experiment will be detailed elsewhere [24].

References
[19] D. Laundy et al., *J. Phys. :Condens. Matter,* **3** (1991) 369.
[20] T. Mizokawa and A. Fujimori, *Phys. Rev. B,* **54** (1996) 5368.
[21] H. Sawada and K. Terakura, *Phys. Rev. B*, **58** (1998) 6831.
[22] H. Ichikawa et al., *Physica B* **281&282** (2000)482.
[23] H. Nakao et al., in preparation.
[24] S. Uemura, H. Maruyama, E. Arakawa and K. Namikawa, in preparation.